Chem

CellPress

Article

Nanoparticle-Based Receptors Mimic Protein-Ligand Recognition

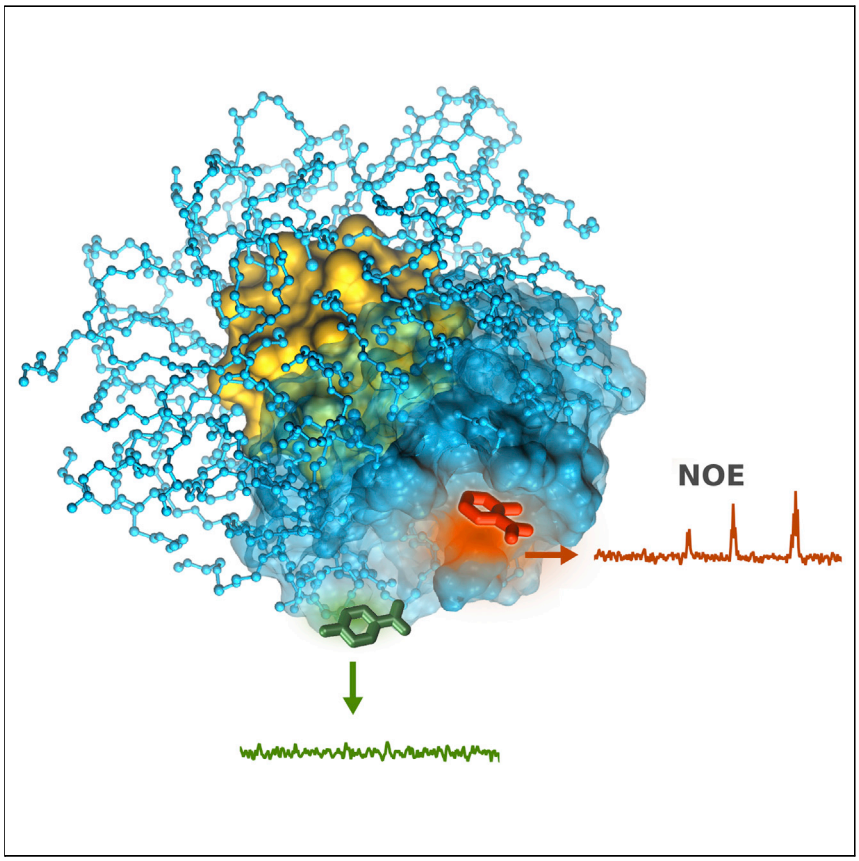

Functionalized gold nanoparticles (AuNPs) can perform different tasks, which depend on the coating ligands that cover the metal core. By combining NMR experiments and molecular-dynamics simulations, De Vivo and colleagues reveal how different ligands can self-organize to modulate molecular recognition ability in AuNPs. Results show how the composition, organization, and plasticity of coating ligands affect the selectivity and sensitivity observed for different organic analytes in NMR chemosensing experiments. These findings offer a unique perspective for the rational design of intelligent nanodevices.

Laura Riccardi, Luca Gabrielli, Xiaohuan Sun, Federico De Biasi, Federico Rastrelli, Fabrizio Mancin, Marco De Vivo

fabrizio.mancin@unipd.it (F.M.)
marco.devivo@iit.it (M.D.V.)

HIGHLIGHTS

Synthesis and molecular simulations of AuNPs for chemosensing

A rationale for the molecular recognition ability of functionalized AuNPs

Functionalized coating ligands form transient protein-like binding pockets

Toward the computational nanodesign of intelligent nanoreceptors for chemosensing

Riccardi et al., Chem *3*, 92–109
July 13, 2017
http://dx.doi.org/10.1016/j.chempr.2017.05.016

Chem

CellPress

Article

Nanoparticle-Based Receptors Mimic Protein-Ligand Recognition

Laura Riccardi,[1] Luca Gabrielli,[2] Xiaohuan Sun,[2] Federico De Biasi,[2] Federico Rastrelli,[2] Fabrizio Mancin,[2,*] and Marco De Vivo[1,3,4,*]

SUMMARY

The self-assembly of a monolayer of ligands on the surface of noble-metal nanoparticles dictates the fundamental nanoparticle's behavior and its functionality. In this combined computational-experimental study, we analyze the structure, organization, and dynamics of functionalized coating thiols in monolayer-protected gold nanoparticles (AuNPs). We explain how functionalized coating thiols self-organize through a delicate and somehow counterintuitive balance of interactions within the monolayer itself and with the solvent. We further describe how the nature and plasticity of these interactions modulate nanoparticle-based chemosensing. Importantly, we found that self-organization of coating thiols can induce the formation of binding pockets in AuNPs. These transient cavities can accommodate small molecules, mimicking protein-ligand recognition, which could explain the selectivity and sensitivity observed for different organic analytes in NMR chemosensing experiments. Thus, our findings advocate for the rational design of tailored coating groups to form specific recognition binding sites on monolayer-protected AuNPs.

INTRODUCTION

The self-assembly of a monolayer of ligands on the surface of noble-metal nanoparticles provides a unique pathway to the realization of ordered and complex molecular structures.[1–4] Within the monolayer, the ligands are aligned, oriented, and kept in close proximity with a particular configuration of the functional groups that are present, which can act cooperatively to perform specific tasks.[5–12] This has been exploited to endow monolayer-protected nanoparticles with the ability to interact with molecular and macromolecular entities, to detect and signal relevant targets, and to catalyze reactions.[13–16] The range of potential applications of such monolayer-protected nanoparticles is therefore huge and spans from materials science and electronics to bioimaging, nanomedicine, and even catalysis.[17,18] In all such applications, molecular recognition is the key point. In a similar way to proteins, the large and organized chemical structure of the monolayer might result in the formation of binding sites in the nanoparticles, which can thereby selectively interact with other entities.[19] Thus, the ultimate goal is now the rational design of nanoparticle-based receptors with programmed selectivity and affinity.[20] To accomplish this, however, several crucial steps must still be taken, in particular, steps toward a deeper understanding of the process of molecular recognition within the nanoparticle-coating monolayer and of the parameters that control it.

In this regard, some of us recently proposed nuclear magnetic resonance (NMR) chemosensing as a protocol that exploits the molecular recognition ability of monolayer-protected gold nanoparticles (AuNPs, about 2 nm core diameter) in order to

The Bigger Picture

The functionalization of monolayer-protected nanoparticles is at the frontier of nanotechnology, such that innovative applications are emerging in fields such as nanomedicine, chemosensing, and even catalysis. Importantly, the nanoparticle's functionality is mainly defined by the nature of the ligands forming the coating monolayer. Here, we show how the self-organization of functionalized coating ligands in monolayer-protected gold nanoparticles (AuNPs) affects their solubility and molecular recognition abilities. We found that coating ligands form transient, protein-like binding pockets in functionalized AuNPs. Thus, we reveal that nanoparticle-based chemosensing operates through a recognition process that is similar to that for protein-ligand complex formation. These findings could now herald the arrival of the computational nanodesign of intelligent nanodevices with recognition abilities toward small molecules such as drugs, metabolites, illegal drugs, and small molecular markers for cancer.

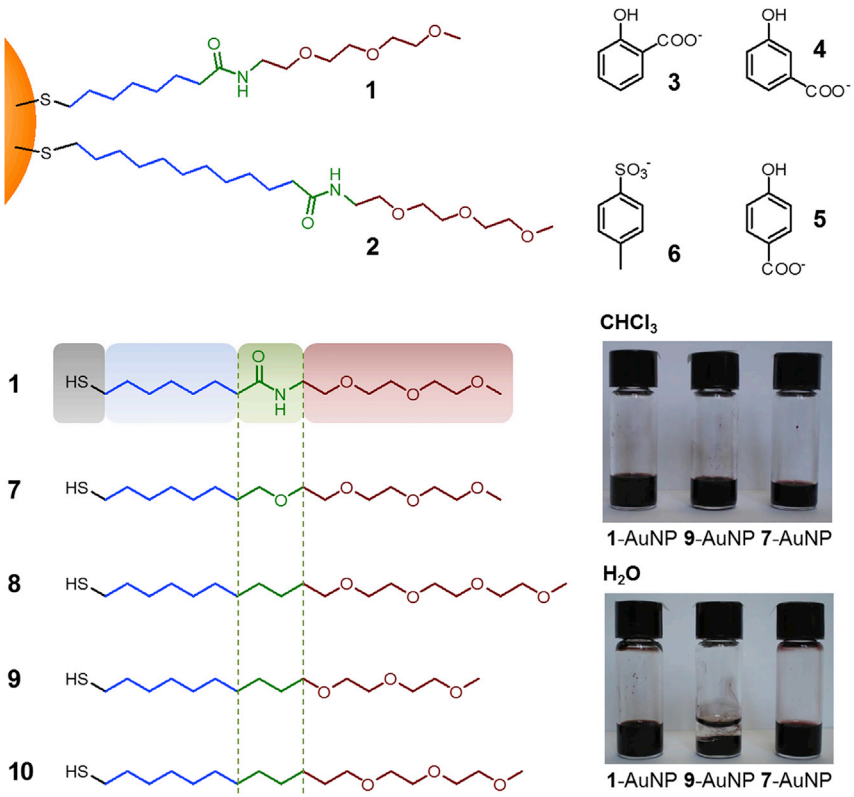

Scheme 1. The NMR Chemosensing Machinery for Analyte Detection

Upper: the monolayer-protected nanoparticles (ligands **1** and **2**) and analytes (**3**–**6**) investigated in early studies.[21]

Lower: nanoparticle-coating thiols (**1** and **7**–**10**) used in this study and the solubility of representative samples in $CHCl_3$ and water.

detect target analytes.[21–24] Typically, these analytes are small organic molecules such as salicylate. This molecular recognition ability for small organic molecules has potential implications for the detection of metabolites, illegal drugs, and molecular markers for cancer, among others. The NMR experiment (nuclear Overhauser effect [NOE] pump)[25] exploits a diffusion filter to dephase the magnetization from all the small molecular species in the sample, followed by an NOE step in which the residual magnetization of the nanoparticles is selectively transferred to the interacting molecules. From an analytical point of view, this experiment allows the NMR spectrum of the target molecule to be isolated even in a complex mixture, revealing its presence and identity. More generally, however, such an experiment also provides detailed information on the molecular recognition ability of the nanoparticles.

Indeed, binding selectivity revealed by earlier experiments was somewhat unexpected. **1**-AuNPs, reported in Scheme 1, detect salicylate (2-hydroxybenzoate, **3**; Scheme 1) in water with a remarkable selectivity with respect to many other aromatic anions of a similar structure, including 3- and 4-hydroxybenzoate (**4** and **5**; Scheme 1) and 4-methylbenzenesulfonate (**6**; Scheme 1).[21] Within this group, salicylate is the molecule with the highest octanol/water partition coefficient (P_{ow}) and the most retained in reversed-phase chromatography. Selective recognition could hence simply arise from the hydrophobic interaction with the inner part of the nanoparticle-coating monolayer. Interestingly, when we elongated the alkyl portion of **1** by four carbon atoms, we obtained **2**-AuNPs (Scheme 1), which could detect

[1]Laboratory of Molecular Modeling & Drug Discovery, Istituto Italiano di Tecnologia, Via Morego 30, 16163 Genova, Italy

[2]Dipartimento di Scienze Chimiche, Università di Padova, Via Marzolo 1, 35131 Padova, Italy

[3]IAS-5/INM-9 Computational Biomedicine Forschungszentrum Jülich, Wilhelm-Johnen-Straße, 52428 Jülich, Germany

[4]Lead Contact

*Correspondence: fabrizio.mancin@unipd.it (F.M.), marco.devivo@iit.it (M.D.V.)

http://dx.doi.org/10.1016/j.chempr.2017.05.016

4-methylbenzenesulfonate in addition to salicylate. Nevertheless, 2-AuNPs could not detect the less hydrophilic 3- and 4-hydroxybenzoate.[21] This result demonstrated that other factors were at play in determining the monolayer's binding selectivity.

In this work, we report a detailed investigation of the recognition abilities of 1-AuNPs and a series of previously unreported monolayer-protected nanoparticles featuring different coating monolayers and selectivity for analytes. NMR-based experiments combined with extensive molecular dynamics (MD) simulations indicate that molecular recognition at the monolayer of these selected AuNPs requires the preformation of specific, although transient, protein-like binding pockets in the nanoparticle-coating monolayer. We found that the presence of these pockets is, in turn, the result of a delicate and somehow counterintuitive balance of interactions within the monolayer itself and with the solvent. Together, these findings represent the basis for the rational design of tailored coating groups that can form selective recognition sites on monolayer-protected AuNPs, which are thus able to operate with programmed recognition ability.[26]

RESULTS AND DISCUSSION

The chemical structure of the original ligand 1 (Scheme 1) can be divided into four parts: (1) the thiol (gray), which ensures the grafting to the monolayer surface; (2) the hydrophobic alkyl chain (blue); (3) an amide group (green), originally inserted for synthetic accessibility;[27] and (4) a hydrophilic oligo(ethylene glycol) (OEG) moiety (red), which ensures water solubility. At first glance, the alkyl part of thiol 1 should be the portion providing relevant interactions with salicylate. In the nanoparticle's coating monolayer, this alkyl part forms a hydrophobic pseudo-phase that can accommodate hydrophobic substrates in a manner similar to that of surfactant aggregates. In addition, the amide group can form additional H bonds (HBs) with the substrate. To better understand these points, we designed a series of analogs where the two relevant parts of the ligand were systematically modified. In all ligands 7–10, the amide group was removed. In 7, it was substituted with an ether group (CH_2O). In this way, the removal of the amide did not substantially affect the size of the alkyl portion, and the ligand maintained the same length as 1. In ligands 8–10, on the other hand, removal of the amide groups was accompanied by an increase in length of the alkyl and/or the OEG portion.

Organization of the Nanoparticle's Coating Monolayer

Ligands 7–10 and the corresponding AuNPs (1.5–1.7 nm gold core diameter) were prepared by standard protocols (Supplemental Information, Sections S1–S3 and S6). Notwithstanding the similar structure of the coating thiols, nanoparticles revealed different solubility properties (Scheme 1 and Supplemental Information, Section S4.1), intended here as the ability to form stable mixtures with the solvent that do not settle upon prolonged storage. Indeed, 1-AuNP was very soluble in water (up to 300 μM or 15 mg/mL) and in organic solvents with high and moderate polarity (from methanol to chloroform).[21,28] 7- and 8-AuNPs were also soluble in water and organic solvents, but saturation concentration in water was lower (about 60 μM or 3 mg/mL) than that of 1-AuNP. Finally, 9- and 10-AuNPs, which contain shorter OEG chains, were soluble only in organic solvents. On the basis of such results, we decided to further investigate the dispersion state of nanoparticles 1-, 7-, and 8-AuNPs in water by transmission electron microscopy (TEM), dynamic light scattering (DLS), and NMR. TEM micrographs obtained by depositing nanoparticle water solutions on the grids showed nanoparticles homogeneously distributed over the substrate, without apparent aggregation (Supplemental Information, Section

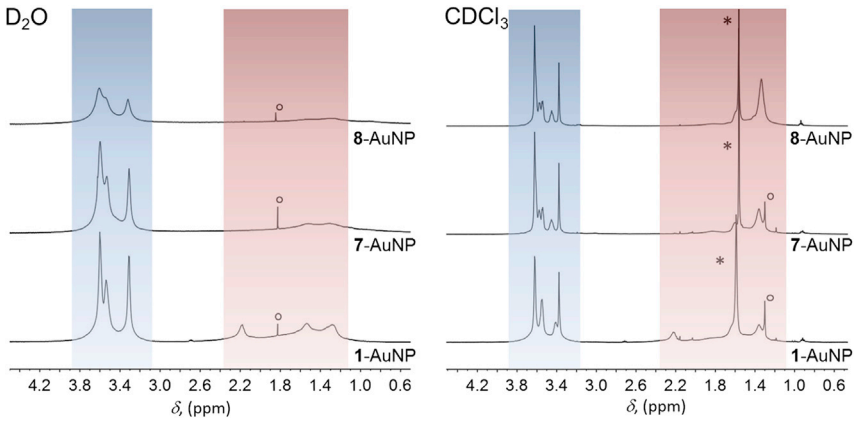

Figure 1. NMR Spectra of 1-, 7-, and 8-AuNP in D_2O and $CDCl_3$

Signals from the OEG portion of the coating thiols are highlighted in blue, and signals from the alkyl portions are highlighted in red. Symbols are as follows: *, residual water signal; and °, impurities.

S4.2). DLS measurements in water (at 15 μM nanoparticle concentration) revealed the presence in each case of a unimodal nanoparticle distribution with average hydrodynamic diameters of 8, 16, and 21 nm for **1**-, **7**-, and **8**-AuNPs, respectively (Supplemental Information, Section S4.3). Similar results were obtained by diffusion-ordered spectroscopy (DOSY)-NMR experiments, which again detected the presence of a unimodal nanoparticle distribution with average hydrodynamic diameters of 5, 15, and 18 nm, respectively (Supplemental Information, Section S4.4). Such results indicated that **1**-AuNPs are present in water solution mainly as isolated nanoparticles, whereas **7**- and **8**-AuNPs form small aggregates. However, both DLS and DOSY-NMR hardly discriminate entities of similar size and consequently cannot provide precise information on the amount of aggregates present in the solutions with respect to isolated nanoparticles. Furthermore, if isolated and aggregated nanoparticles were involved in multiple exchange equilibria (a likely possibility), the interpretation of their apparent diffusivities would be even more complicated. Deeper insight into this point came from ^{1}H NMR investigations (Figure 1).

As expected, because of nanoparticle grafting, all the ^{1}H signals arising from the coating thiols were relatively broad and the hyperfine structure was not resolved.[29] However, a striking difference becomes evident when comparing the spectra recorded in deuterated water for **1**-, **7**-, and **8**-AuNPs (Figure 1). The signals arising from the OEG portion, between 3.3 and 3.8 ppm, and in particular from the terminal methoxy residue at 3.35 ppm, have similar linewidths for **1**-AuNP (13.3 Hz) and **7**-AuNP (16.6 Hz) but are significantly broader for **8**-AuNP (24.5 Hz). Linewidths of signals arising from terminal groups have been shown to strongly depend on nanoparticle size.[30] Indeed, neglecting magnetic field inhomogeneities, NMR signal broadening depends on the transverse relaxation time T_2. This is determined mainly by the dipolar interactions between the spins in the monolayer, as modulated by the nanoparticle tumbling rate and by the internal mobility of the ligands within the monolayer. Because the dynamics of the OEG portions of the coating ligands should be independent from the ligand packing in the monolayer, broadening of **8**-AuNP signals indicates a slower tumbling rate (or chain rigidification) as expected in the case of aggregates. We hence concluded that **7**-AuNPs are dispersed in water mainly as isolated nanoparticles that coexist with a small fraction of aggregates, whereas in the case of **8**-AuNP, the population of aggregates is more pronounced.

Table 1. ^{1}H T_1 and T_2 Relaxation Times for 1-, 7-, and 8-AuNPs in $CDCl_3$ and D_2O

Solvent	Signals	Min–Max T_2 (s)[a]			Min–Max T_1 (s)[a]		
		7-AuNP	8-AuNP	1-AuNP	7-AuNP	8-AuNP	1-AuNP
$CDCl_3$	Alkyl[b]	0.504–0.694	0.429–0.537	0.711–0.766	0.660–0.989	0.667–0.69	1.04–1.30
	OEG[c]	1.12–1.40	0.77–1.37	0.626–0.744	1.17–1.59	0.847–1.64	0.923–0.986
	CH_3[d]	2.61	2.52	1.67	2.84	2.83	1.81
D_2O	Alkyl[b]	0.006**–0.016*	0.024*–0.05*	0.07*–0.11*	0.67–0.7*	0.6**–0.7**	0.596–0.62
	OEG[c]	0.061–0.065	0.031*–0.038*	0.222–0.279	0.648–0.681	0.64–0.64	0.638–0.638
	CH_3[d]	0.101	0.07**	0.52	0.912	0.70	1.13

Errors are within 10% unless indicated: *errors within 25%, **errors within 50%. In cases where the signal decay was found to be multi-exponential, only the largest relaxation times are reported.

[a]For each spectral region, the largest and the smallest relaxation times are reported.

[b]Signals in the 1.2–2.3 ppm range.

[c]Signals in the 3.4–3.8 ppm range.

[d]Broad signal at 3.3 ppm; relaxation parameters for the terminal methyl group are reported separately because they are affected by internal rotation.

Values for ^{1}H relaxation times T_1 and T_2 are reported in Table 1. As expected, T_2 values increase with the distance from the Au core because protons farther from the core are less packed and consequently have larger degrees of freedom with respect to those closer to the nanoparticle core.[5,6,29,30] In $CDCl_3$, T_2 values for the signals of the different regions (alkyl, OEG, CH_3; Table 1) are similar for all AuNPs, confirming that all nanoparticles have a similar mobility of the coating ligands, similar sizes, and are present as isolated entities. In water, the behavior is different; all spins of **1**-AuNP relax more slowly than those of **7**- and **8**-AuNPs.

In the case of **8**-AuNP, such an effect could be ascribed to aggregation that reduces both the nanoparticle tumbling rate and the mobility of the chains (because of their interlocking). However, when **1**- and **7**-AuNP are compared, the decrease in the T_2 values for the latter is much more relevant for the signals arising from the alkyl chains (~10-fold decrease) with respect to the signals from the outer OEG chains (~4-fold decrease). This suggests that, besides a possible reduction of the tumbling rate, faster relaxation of the alkyl signals in **7**-AuNP could also arise from a decrease of their internal mobility. In other words, when in water, the nanoparticles coated with ligands devoid of the amide unit, such as **7**-AuNPs, feature substantially more rigid alkyl chains than those of **1**-AuNP, which contain the amide moiety.

Subsequently, we investigated the ability of water-soluble **1**-, **7**-, and **8**-AuNPs to detect organic molecules with the NMR chemosensing protocol (Figure 2 and Supplemental Information, Section S5). The NOE-pumping sequence was used to analyze samples containing the nanoparticles (15 μM) and salicylate at increasing concentrations (1–10 mM) in carbonate buffered D_2O solution at pD = 10.0. **1**-AuNP confirmed their reported ability to detect salicylate in water.[21] Analyte signals appeared in the NOE-pumping spectra at substrate concentrations as low as 2 mM and increased in both intensity and signal-to-noise ratio with increasing concentration. On the other hand, and surprisingly enough, analyte signals were never detected with a signal-to-noise ratio above 3 (which we usually set as a detection limit) in the experiments performed with **7**- and **8**-AuNPs, even in the presence of high (10 mM) concentrations of the substrate. All the nanoparticles have the same size and a very similar structure of the coating thiols, which leads to similar longitudinal relaxation rates (T_1) of protons within the same moieties (Table 1). Thus, the different signal enhancements observed in NOE-pumping experiments (Figure 2) should rather arise from different cross-relaxation rates, which depend on the affinity

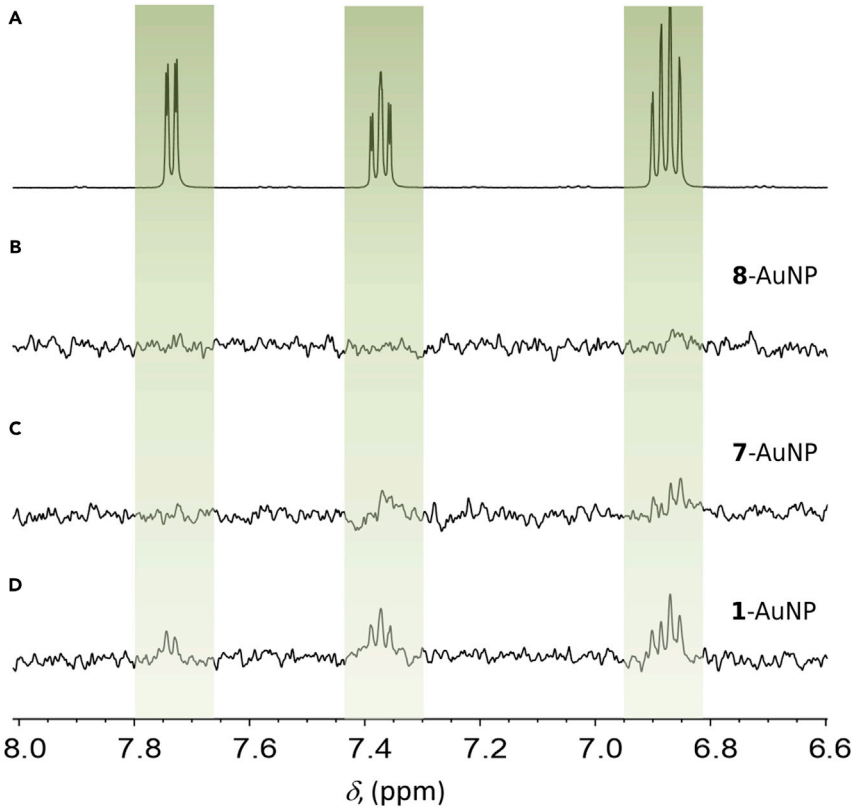

Figure 2. NMR Spectra

(A) ^{1}H NMR subspectrum of 5 mM sodium salicylate (**3**) in D_2O.

(B) NOE-pumping subspectrum of the same sample in the presence of **8**-AuNP.

(C) NOE-pumping subspectrum of the same sample in the presence of **7**-AuNP.

(D) NOE-pumping subspectrum of the same sample in the presence of **1**-AuNP.

Conditions: [AuNP] = 15 μM, carbonate buffer 20 mM, pD = 10, 298 K. See also Supplemental Information Section S5 and Figures S33–S35.

of the analytes for the substrate. This indicates that **7**- and **8**-AuNPs have an affinity for salicylate that is sensibly lower than that of **1**-AuNP and confirms that partition into the hydrophobic pseudo-phase formed by the alkyl portions of the nanoparticles coating thiols cannot explain the observed substrate recognition.

Morphology and Dynamics

On the basis of this evidence, we performed a series of extended MD simulations of all the AuNPs immersed in either explicit water or chloroform. Nanoparticles samples prepared by standard solution methods are usually composed of clusters of different sizes. In our case, the average Au core diameter (1.7 nm) is close to that of the $Au_{144}(SR)_{60}$ cluster[31–34] (~1.6 nm), and the contribution to the observed NOE follows the size distribution (Supplemental Information, Section S7).[35] Indeed, it has already been shown that $Au_{144}(SR)_{60}$ is the main component in nanoparticle batches with average diameter around 2 nm.[35] In addition, we have shown that computational simulations performed with $Au_{144}(SR)_{60}$ nicely predict the properties of nanoparticle samples with similar size distribution.[36] We hence considered the $Au_{144}(SR)_{60}$ structure as a single nanoparticle model to analyze the dynamic properties and interactions of the different coating ligands in explicit solvents through classic MD simulations of >200 ns for each AuNP/solvent system (~3.2 μs in total).

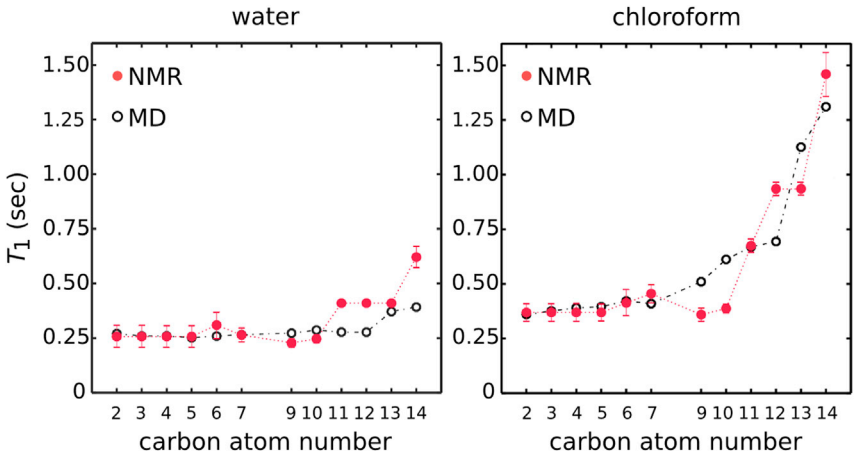

Figure 3. Comparison of Experimental and Calculated T_1 Values of ^{13}C Nuclei along the Chains of 1-AuNPs

Left: **1**-AuNPs dissolved in water.

Right: **1**-AuNPs dissolved in chloroform.

T = 298 K. ^{13}C Larmor frequency = 125.75 MHz. See also Supplemental Information Section S11.6 and Figure S74.

To validate our model systems, we first used the MD simulations to compute the T_1 relaxation times for ^{13}C nuclei of **1**-AuNPs, the only sample soluble enough to allow us to measure the T_1 values for ^{13}C both in deuterated water and $CDCl_3$. In ^{13}C relaxometry experiments, the relaxation of each ^{13}C nucleus depends essentially on the fluctuations of the dipole-dipole interactions between the carbon and the attached protons (neglecting chemical shift anisotropy mechanisms).[37] In this case, relaxation times were calculated on the basis of the MD simulations via the Lipari-Szabo approach (Supplemental Information, Section S11).[38,39] A comparison between the experimental and the MD-calculated T_1 values is reported in Figure 3, which highlights the very good match between the two datasets. The different relaxivities of the carbon nuclei in the two solvents, which in turn depend on the different mobility of the coating chains in the monolayer, are well captured by both our MD simulations and NMR, further supporting the choice of the $Au_{144}(SR)_{60}$ model for the computational studies.

Turning our attention to the picture emerging from the MD simulations, we noticed first that all the monolayer-protected AuNPs were more compact in water, as reflected by a decrease of ~10% in their radius of gyration compared with that in chloroform (Figure 4A). In chloroform, the relative distribution of the three moments of inertia and the eccentricity, which are shape descriptors, indicate that all the AuNPs adopted a spherical shape (Figure 4B). On the contrary, monolayer conformational preferences in water were quite different. **1**- and **7**-AuNP appeared relatively spherical in this solvent too, but we observed progressively broader relative distributions of moments of inertia, causing an increase in the eccentricity values, for **8**-, **9**-, and in particular **10**-AuNPs, suggesting a less spherical shape (Figure 4B). In **10**-AuNP, sphericity deviation can be clearly ascribed to the collapse of the coating molecules into bundles, featuring aligned alkyl chains located at opposite poles of the nanoparticle (Figure 4D).[40] For **7**-, **8**-, and **9**-AuNPs, on the other hand, alkyl chain bundles were not clearly detected, but simulations again indicated a similar level of conformational rigidity for the alkyl portion of these nanoparticles, in line with the broad NMR signals and short transverse relaxation times observed for **7**-AuNP in the NMR experiments (Figure 1 and Table 1). In chloroform, all AuNPs were more

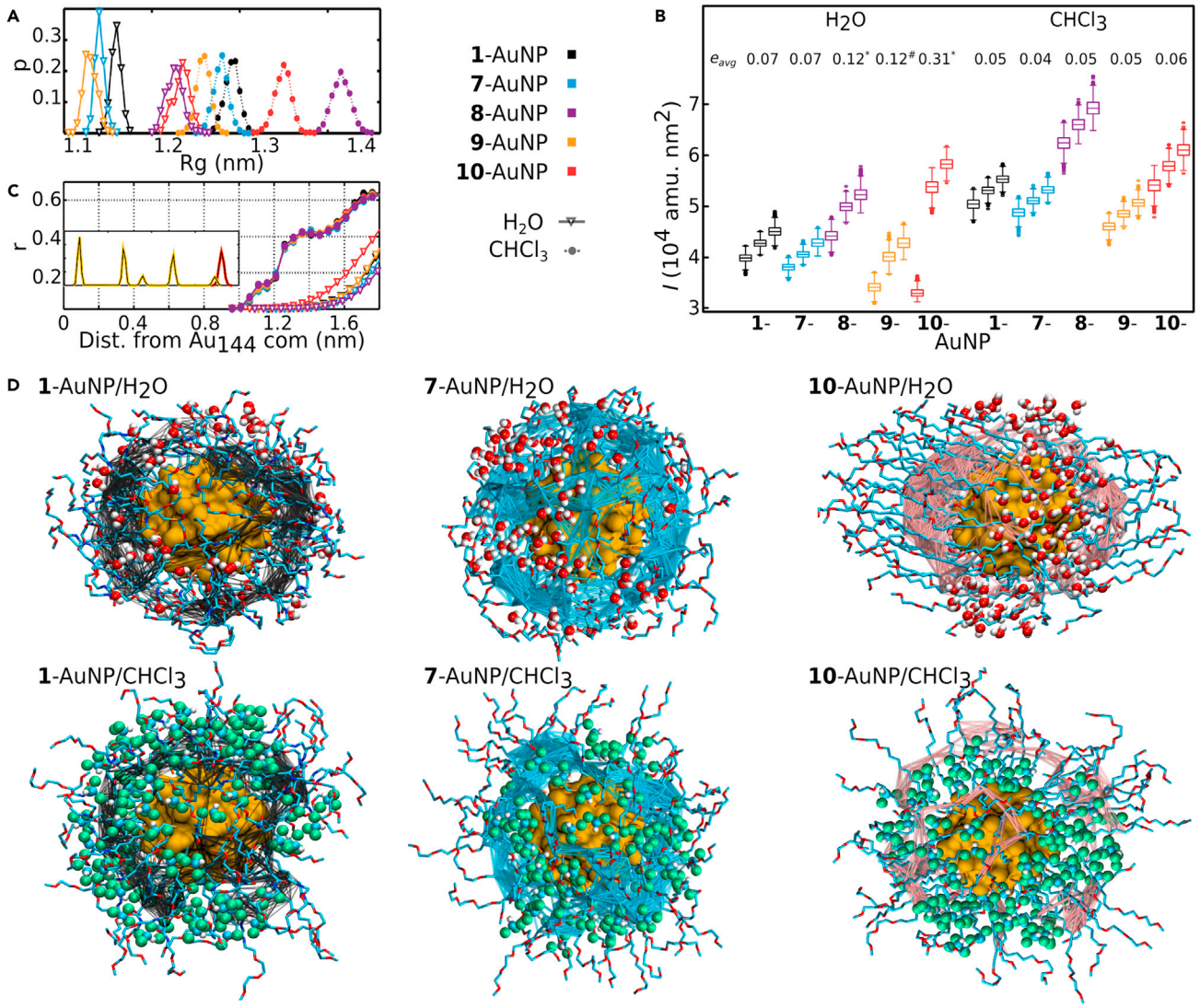

Figure 4. Shape and Solvation of AuNPs

(A and B) Probability distributions of (A) radius of gyration (Rg) and (B) moments of inertia (*I*, shown as box-and-whisker plots) of **1**-, **7**-, **8**-, **9**-, and **10**-AuNPs in water and chloroform. The average nanoparticle eccentricity $e = (1 - I_{min}/I_{avg})$, where $e = 0$ for a sphere and 1 for a prolate spheroid, is also reported (SD = 0.2 except for * and #, where it is 0.3 and 0.4, respectively).

(C) Distribution of the solvent molecules and the gold and sulfur atoms (in the inset in yellow and orange, respectively) from the center of mass of the Au_{144} core.

(D) Representative snapshots of the AuNPs and solvent molecules within 1 nm of the gold atoms (wires connect carbon atoms C^4–C^7 closer than 0.8 nm). See also Supplemental Information Section S11.2 and Figure S70.

flexible than in water, and the OEG of **7**- and **8**-AuNPs was less constrained than that of **1**-AuNP, in agreement with the NMR experiments discussed above.

The elongated spheroid shape of **8**-, **9**-, and **10**-AuNPs in water resulted in exposure of the ligand's alkyl chains to the solvent. This is particularly evident in **10**-AuNPs. Here, the bundling of the coating ligands created a structure with a wide, ring-shaped, equatorial region where alkyl chains were poorly shielded from water by few OEG chains. Indeed, the water molecules closest to the gold core were almost exclusively found in this ring-shaped region (Figure 4D).

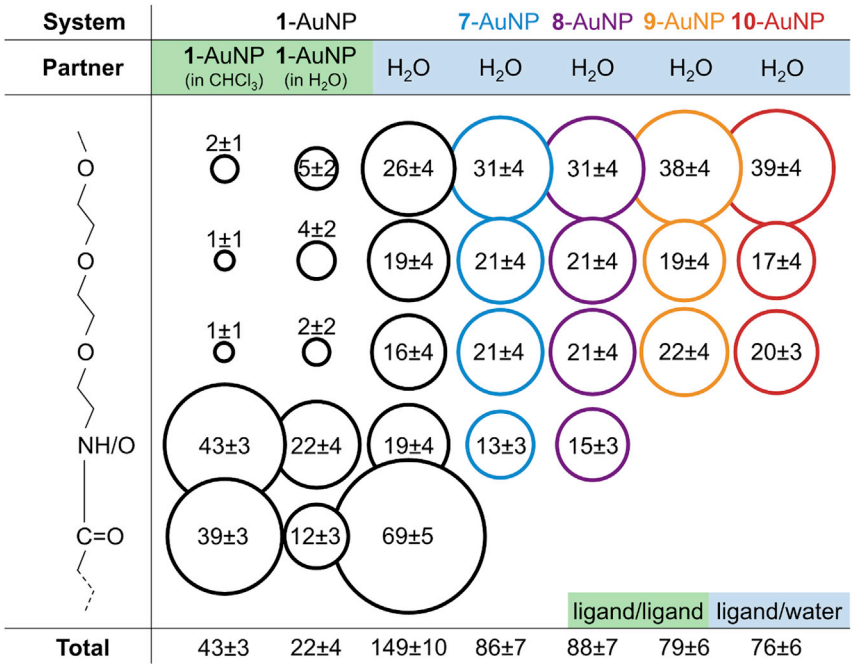

Figure 5. HB Interactions

Average number of ligand-ligand and ligand-water HBs during MD simulations and the decomposition of this number for the different coating thiol atoms (ordered top to bottom from the outer to the inner part of the coating ligand). For NH/O, NH is present in **1**-AuNP and O is present in **7**- and **8**-AuNPs.

The number of ligand-water HBs is reported in Figure 5 and provides interesting information. **1**-AuNP formed the larger number of HBs with the solvent (~150), followed by **7**- and **8**-AuNPs (~86–88) and finally by **9**- and **10**-AuNPs (~76–79).

Interestingly, the trends of the computed eccentricity values in water and of the number of HBs with the solvent well correlate with the observed nanoparticle solubility and aggregation tendency. That is, nanoparticles showing a more spherical shape, with a consequent better shielding of the inner alkyl chains and a better solvation in our simulations, correspond to those present in solution as individual entities. Still, subtle differences found for quite similar nanoparticles, such as **7**- and **8**-AuNP, indicate that a full explanation of nanoparticle stability in solution will require additional investigations.

The substantially greater number of HBs made by **1**-AuNP is due to the amide group, particularly its carbonyl oxygen, which was responsible for ~50% (~60% considering the NH) of the interactions with water. The OEG portion accounts for the remaining 40% of HBs, with the number of interactions decreasing from the terminal and more exposed oxygen to the inner ones. The same trend was observed in **7**-, **8**-, **9**-, and **10**-AuNPs. Here, however, the total number of HBs formed by the three outer oxygens was larger than in **1**-AuNPs (~73–79 versus ~61).

The additional oxygen atom in **7**- and **8**-AuNPs, compared with **9**- and **10**-AuNPs, formed only a few (~13–15) HBs with water. This is because the extra HB acceptor site in **7**- and **8**-AuNPs is buried inside the monolayer and thus poorly exposed to the solvent. In this view, it is striking that the insertion of the carbonyl group in

1-AuNP increased the number of HBs from ~76–79 to ~150. This implies that the amide groups not only provide an additional site of interaction with the solvent, but also substantially affect the conformation of the ligands, which in turn modulate solvation of the monolayer.

Another relevant feature revealed by HB analysis is the interligand interactions in 1-AuNP. In this case, the amide NH group formed 22 ± 4 HBs with acceptors on neighboring ligands. This is quite close to the average number of interactions established with water molecules (19 ± 4). Interestingly, half of the interligand HBs formed by NH are with neighboring carbonyl oxygens, and the remaining ones are formed with the OEG, decreasing from the outer to the inner oxygen (Figure 5). Importantly, these results revealed that: (1) the number of interligand HBs is relatively small (the theoretical maximum being about 60); (2) the formation of HBs between the amide groups and the OEG oxygens is favored by the significant bending of the coating ligands. On the other hand, we found ~90 HBs with intercalated water, which are thus favored compared with interligand HBs. Most likely, HBs with intercalated waters helped maintain the amide groups of 1-AuNP to be spaced and distributed homogeneously, preventing the massive bundling observed with the other AuNPs. Instead, the bending of some ligands of 1-AuNP, which favors rigidification (Figure 3) through interligand HBs with the amide group (Figure 5), explains the smaller average number of interactions that OEG oxygens establish with water, with respect to those formed by 7-, 8-, 9-, and 10-AuNPs.

In chloroform, where HBs with the solvent are not possible, the number of interligand HBs in 1-AuNP almost doubled to 43 ± 3 (Figure 5) in comparison with those in water. At the same time, and in contrast to water, OEG headgroups were rarely involved in these interactions, preferring extended conformations toward the solvent. The interligand HB network generated highly structured HB chains (Figure 6). Such interactions modified the preferred monolayer conformation in these nanoparticles, from the homogeneously distributed structure observed for the simulations in water to a more inhomogeneous structure characterized by the presence of large "canyons" filled by solvent molecules (Figures 4C, 4D, and S70).

Together, these data show that the compactness, shape, and surface arrangement of AuNPs' coating ligands are strongly affected by both the ligand structure and the solvent. In chloroform, ligands prefer a disordered conformation that results in an overall spherical nanoparticle shape. The formation of interligand HBs induces clustering of the ligands in small bundles separated by deep "canyons," only for 1-AuNP. Such a behavior is in full agreement with the early observation by Rotello et al.[41,42] who detected relatively strong interligand HBs in nanoparticles coated with amide-bearing thiols in organic solvents. On the basis of chemical oxidation experiments, such interligand interactions were supposed to generate ligand bundling, and the resulting "canyons" to cause the lower resistance of the gold core to decomposition.[41,42]

In water, it is the dispersive-hydrophobic interaction between the alkyl chains that induces the aggregation of the ligands to form bundles.[5,6] It appears that such structures could favor aggregation and even prevent the nanoparticle's dissolution in water, depending on the length of the OEG chains.

The effect of the amide groups in 1-AuNP in water is therefore somehow intriguingly counterintuitive. Amide groups do not reinforce the bundling, as in chloroform, where they provide an additional interligand interaction.[7] Instead, amide groups

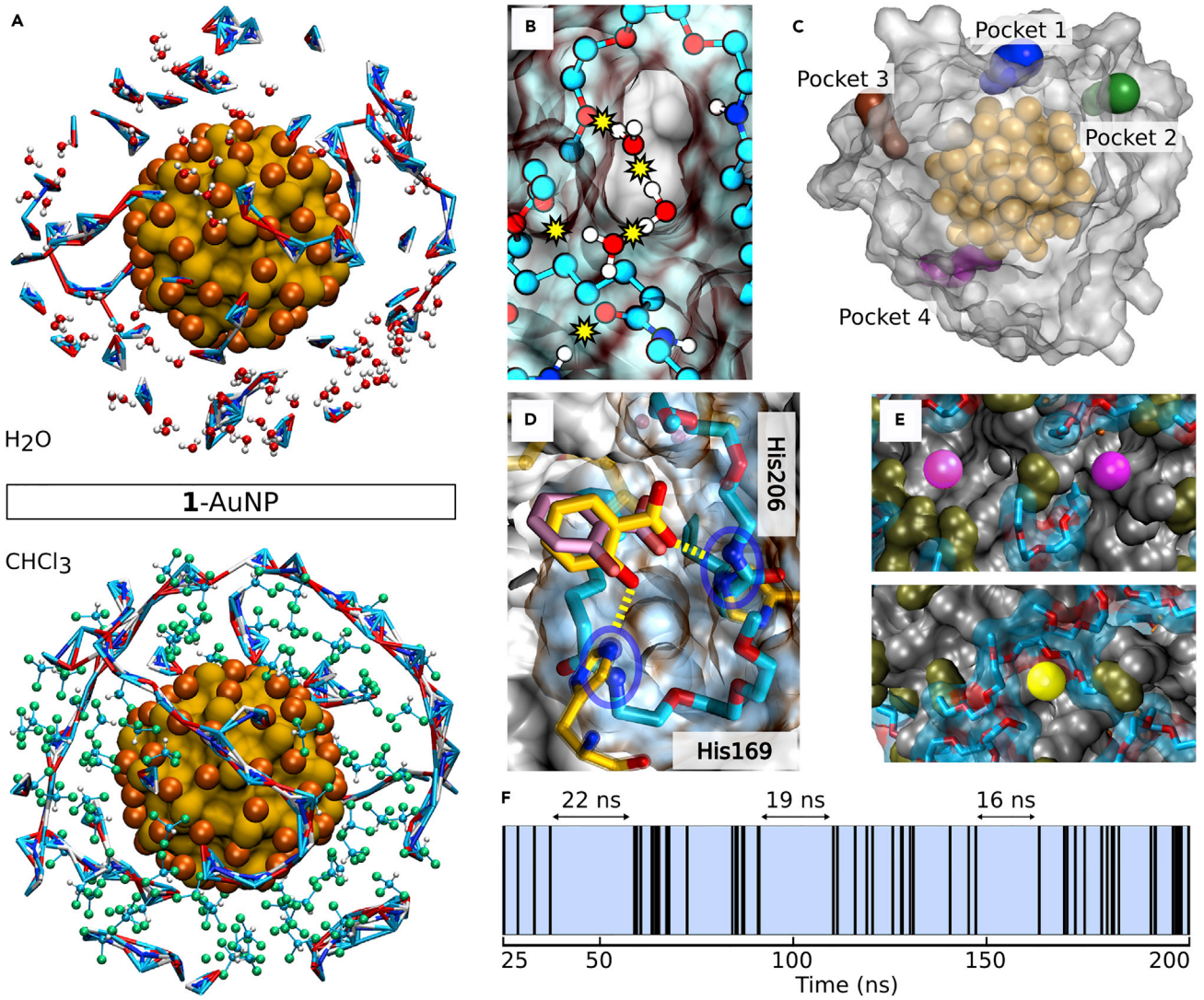

Figure 6. Structure of the Monolayer

(A) Amide group atoms closer than 0.4 nm are connected by wires, and solvent molecules within 1 nm of the Au_{144} core are shown. The Au_{144} core is shown as a gold surface, and sulfur atoms are shown as orange spheres.

(B) Example of the HB network for **1**-AuNP in water.

(C) Identification of pockets on one snapshot of **1**-AuNP in water.

(D) Superposition of the docking pose of salicylate in **1**-AuNP and in the LysR-type transcription factor (PDB: 2Y7K).

(E) Characterization of pockets for **1**-AuNP in water. Magenta spheres indicate the "deep cavity" pockets (left), and yellow spheres indicate the "OEG sinking" pockets (right). Gray, green, and cyan surfaces identify the alkyl, amide, and OEG regions, respectively.

(F) Time evolution and lifetime of a stable pocket formed in **1**-AuNP in water. Blue color for the open pocket and black for the closed pocket.

See also Supplemental Information Sections S11.3–S11.4 and S11.7–S11.8 and Figures S71–72, S75, and S76.

favor the intercalation of water molecules, which act as spacers between the ligands, inducing a more disordered and spherical monolayer conformation in water.

Molecular Basis for Recognition

Importantly, for **1**-, **7**-, and **8**-AuNPs, the simulations in water revealed the formation of transient pockets in the monolayer structure (Figure 6). The pockets showed different sizes and shapes. The observed average number was ~5 ± 2 for each AuNP, and an average volume of ~0.15 ± 0.04 nm^3, which is enough to

accommodate a few waters but also small organic molecules such as salicylate (Supplemental Information, Section S11.7). The lifetime of the pockets ranged from hundreds of picoseconds to tens of nanoseconds, revealing their transient nature. Whereas some pockets were very flexible, i.e., they had a high frequency of transitions between short-lived open and closed conformations, other pockets were more structured and able to remain open for most of the simulation time (see Figure 6F; this pocket was open for >90% of the time). Closer inspection revealed that such pockets could be classified into two different topological classes. The first class, found in all the nanoparticles, was essentially characterized by the sinking of the OEG layer, and only fragments of such moieties composed the pocket walls. The second class, present only in **1**-AuNP, was deeper and penetrated down into the alkyl layer (Figure S76). Notably, in this case, water molecules were often found to form bridges either between distant parts of the same coating ligand (i.e., amide and OEG) or between distinct ligands, creating a complex HB network topology (see Figures 6B and S72).

The occurrence of the latter transient cavities only on the surface of **1**-AuNP helps rationalize the recognition ability of these nanosystems in NMR chemosensing experiments. To further investigate **1**-AuNP's interaction with the bound analytes, we reversed the NOE-pumping approach by transferring magnetization from the analyte to the monolayer with a selective 1D-NOESY pulse scheme.[43] From a qualitative viewpoint, the larger the number of close contacts between the monolayer and the analyte, the stronger the nanoparticles' NOE signals in this experiment. The 1D-NOESY spectrum in Figure 7 clearly shows that NOE enhancements on the alkyl portion of the coating monolayer are larger than those on the oxymethylene moieties. This suggests that the salicylate molecule arranges in such a way as to place its protons in close proximity to the inner alkyl portion of the monolayer. However, its position in the monolayer is not deep enough to prevent contacts with the OEG portion, as demonstrated by the weak NOE signals observed.

This result was compared with molecular docking calculations of salicylate to the four pockets detected on the monolayer of a representative equilibrated MD snapshot (Figure 6). In particular, pockets 1 and 2 were of the "deep cavity" type, and pockets 3 and 4 were of the "OEG sinking" type. Interestingly, we found that the interaction network of the salicylate's docking pose into pockets 1 and 2 gave rise to a large number of contacts with the alkyl portion of the coating ligand (Figure 7C), in agreement with the results of the selective NOESY experiment. On the other hand, docking in pockets 3 and 4 resulted in predominant contacts with the OEG groups (Figure S78). There is thus a good qualitative agreement between the NMR data and the docking of salicylate to the "deep cavity" pockets that are present in **1**-AuNPs. In addition, the predicted docking pose into pocket 2 well matched that of salicylate co-crystallized with LysR-type transcription factors (Figure 6D).[44] This corroborates the idea that AuNPs can form protein-like pockets on the surface, as here in **1**-AuNP, and suggests that cavities with the proper topology are essential for the specific interaction with selected analytes. Nicely enough, Lucarini et al.[45] have reported that AuNPs coated with thiol **1** undergo a decrease of affinity for hydrophobic organic molecules as their size increases. Indeed, formation of binding pockets in the monolayer would be more difficult in large nanoparticles, as the decreased curvature should induce a stronger packing of the thiols, which in turn could hamper pockets opening.

Accommodation of the substrate inside pockets in the nanoparticle-coating monolayer is somewhat expected. The different efficiency of **1**- and **7**-AuNPs in the

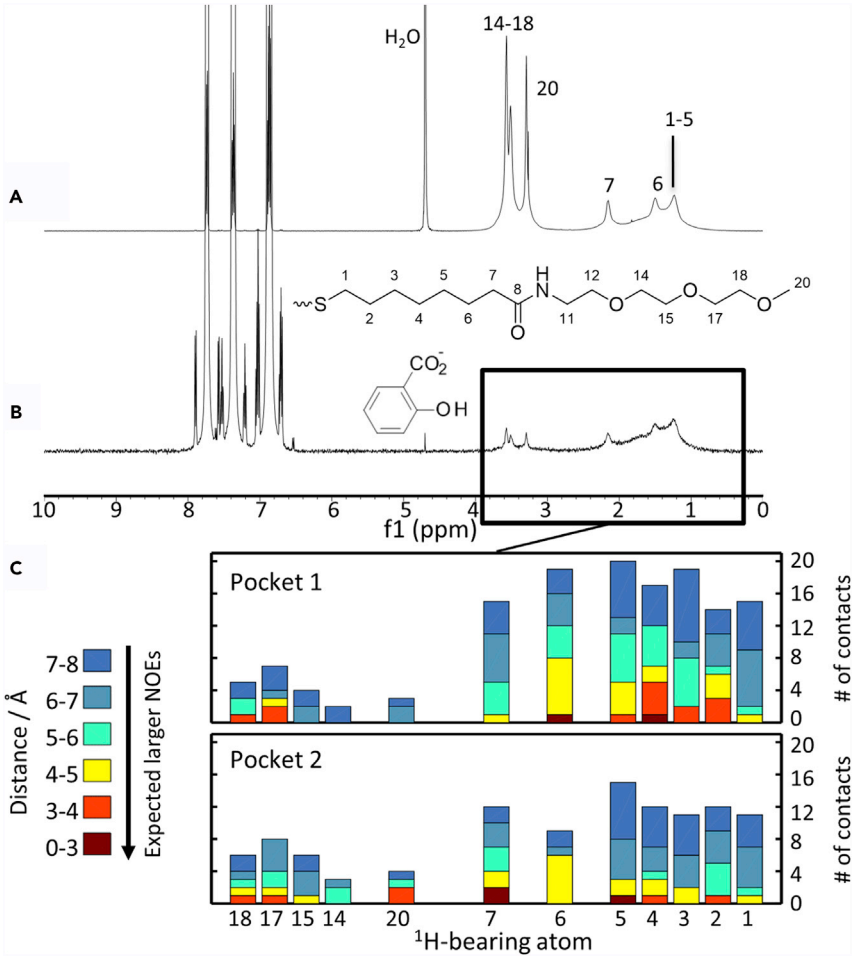

Figure 7. Interactions between Analyte and AuNP

(A) ^{1}H reference spectrum of 20 mM sodium salicylate and 10 mM **1**-AuNP in D_2O carbonate buffer (pD = 10).

(B) 1D NOESY spectrum of the same sample obtained with selective excitation of the salicylate resonances (6–9 ppm) and 300-ms mixing time. Signals of the nanoparticle highlight a negative NOE regime (slow tumbling).

(C) Number of total ^{1}H-^{1}H contacts, color coded in intervals of 1 Å, between docked salicylate and ^{1}H-bearing atoms of **1**-AuNP (exchangeable NH omitted). The bars have been sorted according to the chemical shifts of the parent atoms.

See also Supplemental Information Section S12 and Figure S78.

NOE-pumping experiments, however, indicates that pocket opening might be a prerequisite for an efficient recognition. To clarify these relevant points and define the molecular basis for the AuNP- and analyte-recognition process, we ran two 1-μs-long MD simulations of **1**-AuNP, with either salicylate or 4-hydroxybenzoate (**3** or **5** in Scheme 1, respectively) in solution. The results showed that salicylate, which is selectively detected by **1**-AuNP in chemosensing experiments (Figure 8A), spent ~48% of the simulation time bound to the monolayer (i.e., conformations in which the distance between protons of the analyte and of the monolayer was less than 0.4 nm). In addition, residence time related to each recognition event was quite long, lasting tens of nanoseconds (Figure 8B). In NOE-pumping experiments, a sizable magnetization transfer between the spins of the monolayer and those of the analyte is detected only when the residence time of the analyte in the monolayer

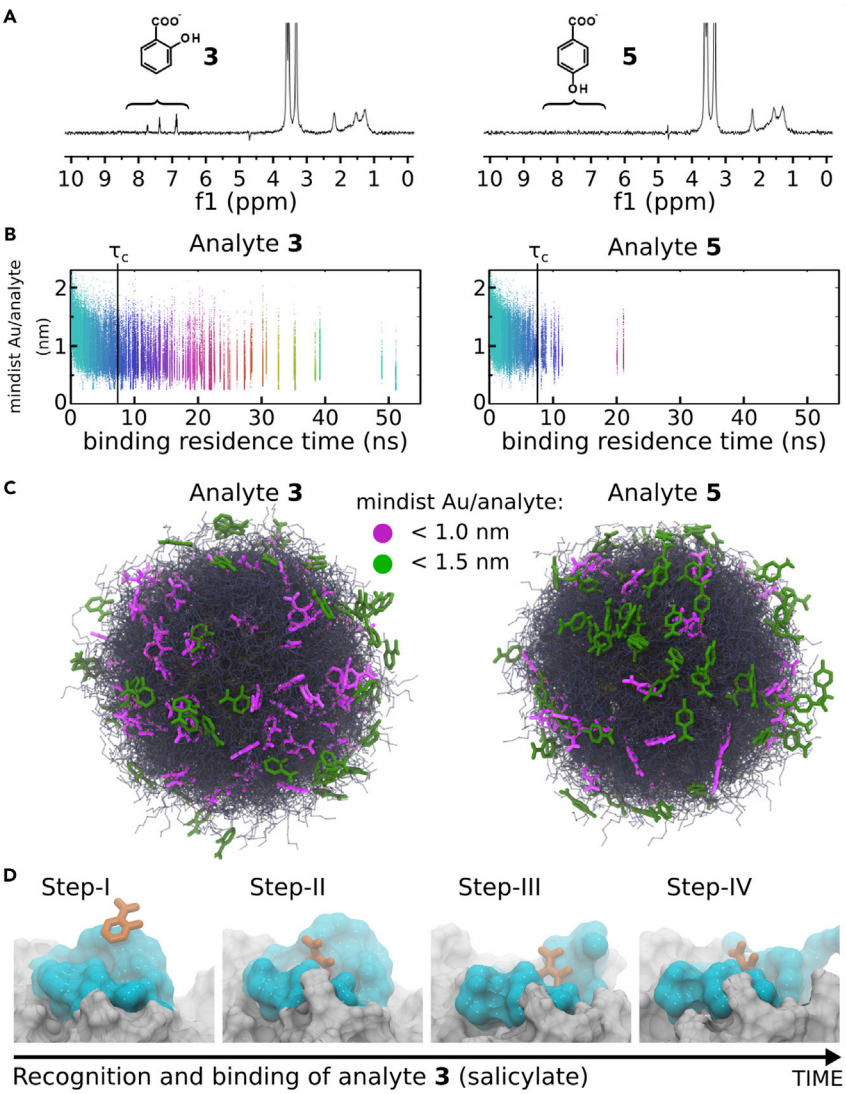

Figure 8. 1-AuNP-Analyte Interactions

(A) NOE-pumping spectra resulting from a solution of 15 μM **1**-AuNP with either 5 mM salicylate (left) or 5 mM 4-hydroxybenzoate (right). Mixing time is 1.2 s. The emergence of a signal only for salicylate is well rationalized by the MD results outlined in (B) (see text for details).

(B) During MD simulations, **1**-AuNP-analyte binding events were defined when the minimum intermolecular proton-proton distance was less than 0.4 nm. The binding events were sorted by their binding residence time (x coordinate) and plotted against the minimum distance between the analyte and the Au_{144} core (depth of penetration in the monolayer, y coordinate). The rotational correlation time (τ_c) of **1**-AuNP is also reported as a visual guideline.

(C) Distribution of the analytes in the monolayer taken from MD snapshots every 25 ns. Purple analytes lie at max 1 nm from the gold core, and green analytes lie between 1 and 1.5 nm.

(D) Binding event of salicylate to **1**-AuNP.

See also Supplemental Information Section S11.9, Figure S77, and Movie S1.

is comparable, or longer, than the rotational correlation time (τ_c) of the nanoparticle.[24] Inspection of Figure 8B, where the binding events are sorted according to their binding residence time, reveals that many binding events of salicylate visibly exceed τ_c of the nanoparticle. Moreover, in agreement with NOE experiments, MD simulations indicated that salicylate was mostly sinking into the inner part of

the monolayer, with the aromatic ring pointing toward the gold core and the carboxylate group remaining exposed to the water solution (Figure S77). We also detected the formation of HBs between the substrate's carboxylate and hydroxyl groups and the monolayer amides, which were formed during 6% of the total simulation time.

On the other hand, 4-hydroxybenzoate, which is not experimentally detected by NOE-pumping experiments with **1**-AuNP (Figure 8A), was in the bound state only for 27% of the overall simulation time. Moreover, the observed binding events of 4-hydroxybenzoate were on a short timescale (a few nanoseconds), thus rarely above τ_c. Indeed, our MD simulations show that this analyte was mostly floating on the outer OEG surface compared with salicylate. Orientation of 4-hydroxybenzoate inside the monolayer was similar to that observed for salicylate, with the carboxylate group pointing toward the water phase. In this configuration, the 4-hydroxy group is located deep inside the hydrophobic portion of the cavity. Such unfavorable conditions most likely justify the shorter permanence of the substrate into the cavities.

Noticeably, the time of residence into the cavities is not only correlated with magnetization transfer but also with binding affinity, because it directly depends on the rate of dissociation (k_{off}) of the analytes from the monolayer. Hence, a longer residence time suggests a higher thermodynamic affinity of the substrate for the monolayer.

Ultimately, these simulations allowed us to decipher the binding mechanism of salicylate to **1**-AuNP, which occurred through four main steps (Figure 8D and Movie S1): (I) formation of transient pockets in the monolayer; (II) binding of salicylate into one of these transient pockets; (III) conformational changes of the pocket in response to analyte binding; (IV) sinking of the analyte into the inner shell of the monolayer. Such a sequence confirms our early hypothesis that the opening of the pocket is the essential prerequisite for ligand binding. Consequently, as found here, the recognition ability of nanoparticles is crucially related to their ability to form pockets with the proper structure and lifetime. Fascinatingly, the series of events listed able also suggests an interplay between conformational selection and induced fit,[46] well mimicking the recognition and binding process for protein-ligand complex formation.

Conclusions

Overall, this combined computational-experimental study shows that functionalized coating ligands can self-organize through a delicate and somehow counterintuitive balance of interactions within the monolayer itself and with the solvent. We demonstrate that these complex interactions can also favor the formation of transient, protein-like binding pockets in monolayer-protected AuNPs, which has so far only been hypothesized.[19,47] These findings imply that nanoparticle-based recognition operates through a process that is similar to that for protein-ligand complex formation. The investigation method designed here, which conjugates detailed NMR studies and atomistic MD simulations, could find application in any nanoparticle-based recognition event. The results reported here also raise new questions that merit further investigation, e.g., which structural and physiochemical parameters predominantly control monolayer organization and pocket formation, similar to that established for binding pockets in proteins. This might help the rational design of thiols capable of favoring the formation of selective pockets and receptors in the nanoparticle-coating monolayer. Addressing such stimulating problems could herald the arrival of the computational nanodesign of new functionalized nanoreceptors with programmed recognition ability.

EXPERIMENTAL PROCEDURES

Nanoparticle Synthesis

Thiols **7**–**10** were synthesized by standard procedures (Supplemental Information, Sections S1 and S2). AuNPs were prepared by chemical reduction of $HAuCl_4$ according to a two-phase, two-step protocol (Supplemental Information, Section S3).[48] In brief, tetracloroaurate was extracted in toluene with tetraoctylammonium bromide as the phase-transfer agent. The nanoparticles were formed by reduction with $NaBH_4$ in the presence of dioctylamine as stabilizer. In situ exchange of the amine with thiols provided the nanoparticles. AuNPs were characterized by TEM, thermogravimetric analysis, UV-visible spectroscopy, and NMR. The average diameter of the gold cores was 1.5–1.7 nm (σ = 0.2 nm). The average nanoparticle formula, calculated over all the AuNPs, was $Au_{137}(SR)_{58}$, suggesting that the samples mainly comprised $Au_{144}(SR)_{60}$ clusters (~1.6 nm; see Negishi et al.[35]).

NMR Experiments

NMR experiments were performed on a Bruker AVIII 500 equipped with a 5 mm *z*-gradient BBI probe. ^{1}H relaxation times were measured at 500.13 MHz Larmor frequency with standard CPMG (T_2) and inversion recovery (T_1) pulse sequences. NOE-pumping experiments were performed with the pulse sequence detailed in Perrone et al.[21] and Salvia et al.[22] ^{13}C T_1 relaxation times were obtained at 125.75 MHz Larmor frequency by inversion recovery under proton decoupling conditions[37] on a Bruker AVANCE DRX 500 equipped with a 5 mm *z*-gradient TCI ^{1}H-$^{13}C/^{15}N/^{2}H$ cryoprobe.

MD Simulations

The three-dimensional structure of the simulated AuNPs is based on the $Au_{144}(SR)_{60}$ model of Lopez-Acevedo et al.,[31] which is the main component in our experimental nanoparticle batches. Although this model does not account for size dispersion, it is responsible for most of the effect observed in our experiments (see Results and Supplemental Information, Section S7). We have already shown that simulations performed with this model nicely reproduce the behavior of nanoparticles samples with an average diameter of 1.6–1.8 nm.[36] The coating groups, as well as salicylate and 4-hydroxybenzoate (**3** and **5** in Scheme 1), were parametrized with GAFF[49] and the atomic charges were derived by the RESP fitting procedure[50] by a force-field topology database-building approach as developed in RedServer.[51] The van der Waals parameters for the gold atoms were taken from Heinz et al.[52] The AuNPs were first minimized via the steepest descent algorithm in a vacuum. Then, the simulation box was built to ensure a minimum distance between the AuNPs and the box edges of at least 1 nm and filled up with either water (TIP3P model) or chloroform molecules. For **1**-AuNP, further simulations were carried out with explicit analytes at a concentration of 35 mM. A second minimization was applied to relax the solvent molecules around the solute. The system was then thermalized and pressurized in different steps. After this initial phase, the system was ready for productive MD simulations. Production runs were carried out in the NPT (p = 1 bar, T = 300 K) statistical ensemble. All bonds were constrained with LINCS, allowing a time-step set of 2 fs. Periodic boundary conditions were applied to the systems in all directions. The PME method was used to evaluate long-range electrostatic interactions, and a cutoff of 10 Å was used to account for the van der Waals interactions (full protocol in Supplemental Information, Sections S9 and S10). All MD simulations were performed with GROMACS-4.6.[53] Coordinates of the systems were collected every 2 ps, and the analysis was performed every 100 ps. All analyses reported refer to the simulations after 25 ns of equilibration. The simulation time was >200 ns for each AuNP-solvent

system (~3.2 μs in total) and 1 μs for each of the two **1**-AuNP-analyte systems (20 μs of a single analyte-AuNP interaction in total).

SUPPLEMENTAL INFORMATION

Supplemental Information includes Supplemental Experimental Procedures, 78 figures, 2 tables, 5 schemes, and 1 movie and can be found with this article online at http://dx.doi.org/10.1016/j.chempr.2017.05.016.

AUTHOR CONTRIBUTIONS

Experimental work was conducted by L.G., X.S., F.D.B., F.R., and F.M. Computational work was conducted by L.R. and M.D.V. All authors analyzed the results. L.R., F.R., F.M., and M.D.V. co-wrote the manuscript.

ACKNOWLEDGMENTS

Financial support was provided by the Italian Association for Cancer Research through investigator grant no. 18883 to M.D.V., by the European Research Council through Starting Grant "MOSAIC" (no. 259014) to F.M., and by the University of Padova through the Progetto Strategico di Ateneo NAMECA. X.S. thanks the China Scholarship Council for a PhD fellowship. Access to the Centro di Risonanze Magnetiche (CERM) infrastructure (Florence) provided by Mario Piccioli and technical support from Fabio Calogiuri are gratefully acknowledged.

Received: December 7, 2016
Revised: March 20, 2017
Accepted: May 24, 2017
Published: July 13, 2017

REFERENCES AND NOTES

1. Gentilini, C., Franchi, P., Mileo, E., Polizzi, S., Lucarini, M., and Pasquato, L. (2009). Formation of patches on 3D SAMs driven by thiols with immiscible chains observed by ESR spectroscopy. Angew. Chem. Int. Ed. *48*, 3060–3064.

2. Stewart, A., Zheng, S., McCourt, M.R., and Bell, S.E.J. (2012). Controlling assembly of mixed thiol monolayers on silver nanoparticles to tune their surface properties. ACS Nano *6*, 3718–3726.

3. Shaw, C.P., Fernig, D.G., and Lévy, R. (2011). Gold nanoparticles as advanced building blocks for nanoscale self-assembled systems. J. Mater. Chem. *21*, 12181–12187.

4. Della Sala, F., and Kay, E.R. (2015). Reversible control of nanoparticle functionalization and physicochemical properties by dynamic covalent exchange. Angew. Chem. Int. Ed. *54*, 4187–4191.

5. Badia, A., Singh, S., Demers, L., Cuccia, L., Brown, G.R., and Lennox, R.B. (1996). Self-assembled monolayers on gold nanoparticles. Chem. A. Eur. J. *2*, 359–363.

6. Badia, A., Gao, W., Singh, S., Demers, L., Cuccia, L., and Reven, L. (1996). Structure and chain dynamics of alkanethiol-capped gold colloids. Langmuir *12*, 1262–1269.

7. Schmitt, H., Badia, A., Dickinson, L., Reven, L., and Lennox, R.B. (1998). The effect of terminal hydrogen bonding on the structure and dynamics of nanoparticle self-assembled monolayers (SAMs): an NMR dynamics study. Adv. Mater. *10*, 475–480.

8. Boal, A.K., and Rotello, V.M. (2000). Fabrication and self-optimization of multivalent receptors on nanoparticle scaffolds. J. Am. Chem. Soc. *122*, 734–735.

9. Quarta, A., Curcio, A., Kakwere, H., and Pellegrino, T. (2012). Polymer coated inorganic nanoparticles: tailoring the nanocrystal surface for designing nanoprobes with biological implications. Nanoscale *4*, 3319–3334.

10. Conde, J., Dias, J.T., Grazú, V., Moros, M., Baptista, P.V., and de la Fuente, J.M. (2014). Revisiting 30 years of biofunctionalization and surface chemistry of inorganic nanoparticles for nanomedicine. Front. Chem. *2*, 1–27.

11. Liu, X., Hu, Y., and Stellacci, F. (2011). Mixed-ligand nanoparticles as supramolecular receptors. Small *7*, 1961–1966.

12. Ghosh, P.S., Verma, A., and Rotello, V.M. (2007). Binding and templation of nanoparticle receptors to peptide α-helices through surface recognition. Chem. Commun. 2796–2798.

13. Mancin, F., Scrimin, P., and Tecilla, P. (2012). Progress in artificial metallonucleases. Chem. Commun. *48*, 5545–5559.

14. Daniel, M.C.M., and Astruc, D. (2004). Gold nanoparticles: assembly, supramolecular chemistry, quantum-size related properties and applications toward biology, catalysis and nanotechnology. Chem. Rev. *104*, 293–346.

15. Lin, C., Yeh, Y., Yang, C., Chen, C.-L., Chen, G.-F., Chen, C., and Wu, Y. (2002). Selective binding of mannose-encapsulated gold nanoparticles to type 1 pili in *Escherichia coli*. J. Am. Chem. Soc. *124*, 3508–3509.

16. Van Lehn, R.C., Ricci, M., Silva, P.H.J., Andreozzi, P., Reguera, J., Voïtchovsky, K., Stellacci, F., and Alexander-Katz, A. (2014). Lipid tail protrusions mediate the insertion of nanoparticles into model cell membranes. Nat. Commun. *5*, 4482.

17. Giljohann, D.A., Seferos, D.S., Daniel, W.L., Massich, M.D., Patel, P.C., and Mirkin, C.A. (2010). Gold nanoparticles for biology and medicine. Angew. Chem. Int. Ed. *49*, 3280–3294.

18. Dreaden, E.C., Alkilany, A.M., Huang, X., Murphy, C.J., and El-Sayed, M.A. (2012). The golden age: gold nanoparticles for biomedicine. Chem. Soc. Rev. *41*, 2740–2779.

19. Kotov, N.A. (2010). Inorganic nanoparticles as protein mimics. Science *330*, 188–189.

20. Pezzato, C., Maiti, S., Chen, J.L.-Y., Cazzolaro, A., Gobbo, C., and Prins, L.J. (2015). Monolayer protected gold nanoparticles with metal-ion binding sites: functional systems for

chemosensing applications. Chem. Commun. (Camb.) *51*, 9922–9931.

21. Perrone, B., Springhetti, S., Ramadori, F., Rastrelli, F., and Mancin, F. (2013). "NMR chemosensing" using monolayer-protected nanoparticles as receptors. J. Am. Chem. Soc. *135*, 11768–11771.

22. Salvia, M.-V., Salassa, G., Rastrelli, F., and Mancin, F. (2015). Turning supramolecular receptors into chemosensors by nanoparticle-assisted "NMR chemosensing". J. Am. Chem. Soc. *137*, 11399–11406.

23. Guarino, G., Rastrelli, F., Scrimin, P., and Mancin, F. (2012). Lanthanide-based NMR: a tool to investigate component distribution in mixed-monolayer-protected nanoparticles. J. Am. Chem. Soc. *134*, 7200–7203.

24. Salvia, M., Ramadori, F., Springhetti, S., Diez-Castellnou, M., Perrone, B., Rastrelli, F., and Mancin, F. (2015). Nanoparticle-assisted NMR detection of organic anions: from chemosensing to chromatography. J. Am. Chem. Soc. *137*, 886–892.

25. Chen, A., and Shapiro, M.J. (1998). NOE pumping: a novel NMR technique for identification of compounds with binding affinity to macromolecules. J. Am. Chem. Soc. *120*, 10258–10259.

26. Su, S., Zuo, X., Pan, D., Pei, H., Wang, L., Fan, C., and Huang, W. (2013). Design and applications of gold nanoparticle conjugates by exploiting biomolecule–gold nanoparticle interactions. Nanoscale *5*, 2589–2599.

27. Pengo, P., Polizzi, S., Battagliarin, M., Pasquato, L., and Scrimin, P. (2003). Synthesis, characterization and properties of water-soluble gold nanoparticles with tunable core size. J. Mater. Chem. *13*, 2471–2478.

28. Lucarini, M., and Pasquato, L. (2010). ESR spectroscopy as a tool to investigate the properties of self-assembled monolayers protecting gold nanoparticles. Nanoscale *2*, 668–676.

29. Terrill, R.H., Postlethwaite, T.A., Chen, C., Poon, C.-D., Terzis, A., Chen, A., Hutchison, J.E., Clark, M.R., and Wignall, G. (1995). Monolayers in three dimensions: NMR, SAXS, thermal, and electron hopping studies of alkanethiol stabilized gold clusters. J. Am. Chem. Soc. *117*, 12537–12548.

30. Hostetler, M.J., Wingate, J.E., Zhong, C.-J., Harris, J.E., Vachet, R.W., Clark, M.R., Londono, J.D., Green, S.J., Stokes, J.J., Wignall, G.D., et al. (1998). Alkanethiolate gold cluster molecules with core diameters from 1.5 to 5.2 nm: core and monolayer properties as a function of core size. Langmuir *14*, 17–30.

31. Lopez-Acevedo, O., Akola, J., Whetten, R.L., Grönbeck, H., and Häkkinen, H. (2009). Structure and bonding in the ubiquitous icosahedral metallic gold cluster $Au_{144}(SR)_{60}$. J. Phys. Chem. C *113*, 5035–5038.

32. Heikkilä, E., Gurtovenko, A.A., Martinez-Seara, H., Häkkinen, H., Vattulainen, I., and Akola, J. (2012). Atomistic simulations of functional $Au_{144}(SR)_{60}$ gold nanoparticles in aqueous environment. J. Phys. Chem. C *116*, 9805–9815.

33. Simonelli, F., Bochicchio, D., Ferrando, R., and Rossi, G. (2015). Monolayer-protected anionic Au nanoparticles walk into lipid membranes step by step. J. Phys. Chem. Lett. *6*, 3175–3179.

34. Whetten, R.L., and Price, R.C. (2007). Nano-golden order. Science *318*, 407–408.

35. Negishi, Y., Nakazaki, T., Malola, S., Takano, S., Niihori, Y., Kurashige, W., Yamazoe, S., Tsukuda, T., and Häkkinen, H. (2015). A critical size for emergence of nonbulk electronic and geometric structures in dodecanethiolate-protected Au clusters. J. Am. Chem. Soc. *137*, 1206–1212.

36. Piserchia, A., Zerbetto, M., Salvia, M.-V., Salassa, G., Gabrielli, L., Mancin, F., Rastrelli, F., and Frezzato, D. (2015). Conformational mobility in monolayer-protected nanoparticles: from torsional free energy profiles to NMR relaxation. J. Phys. Chem. C *119*, 20100–20110.

37. Kowalewski, J., and Mäler, L. (2006). Nuclear Spin Relaxation in Liquids: Theory, Experiments, and Applications (Taylor & Francis), p. 426.

38. Lipari, G., and Szabo, A. (1982). Model-free approach to the interpretation of nuclear magnetic resonance relaxation in macromolecules. 1. Theory and range of validity. J. Am. Chem. Soc. *104*, 4546–4559.

39. Clore, G.M., Szabo, A., Bax, A., Kay, L.E., Driscoll, P.C., and Gronenborn, A.M. (1990). Deviations from the simple two-parameter model-free approach to the interpretation of nitrogen-15 nuclear magnetic relaxation of proteins. J. Am. Chem. Soc. *112*, 4989–4991.

40. Luedtke, W.D., and Landman, U. (1996). Structure, dynamics, and thermodynamics of passivated gold nanocrystallites and their assemblies. J. Phys. Chem. *100*, 13323–13329.

41. Boal, A.K., and Rotello, V.M. (2000). Intra - and Inter monolayer hydrogen bonding in amide-functionalized alkanethiol self-assembled monolayers on gold nanoparticles. Langmuir *16*, 9527–9532.

42. Briggs, C., Norsten, T.B., and Rotello, V.M. (2002). Inhibition and acceleration of deuterium exchange in amide-functionalized monolayer-protected gold clusters. Chem. Commun. *3*, 1890–1891.

43. Stott, K., Keeler, J., Van, Q.N., and Shaka, A.J. (1997). One-dimensional NOE experiments using pulsed field gradients. J. Magn. Reson. *125*, 302–324.

44. Devesse, L., Smirnova, I., Lönneborg, R., Kapp, U., Brzezinski, P., Leonard, G.A., and Dian, C. (2011). Crystal structures of DntR inducer binding domains in complex with salicylate offer insights into the activation of LysR-type transcriptional regulators. Mol. Microbiol. *81*, 354–367.

45. Lucarini, M., Franchi, P., Pedulli, G.F., Gentilini, C., Polizzi, S., Pengo, P., Scrimin, P., and Pasquato, L. (2005). Effect of core size on the partition of organic solutes in the monolayer of water-soluble nanoparticles: an ESR investigation. J. Am. Chem. Soc. *127*, 16384–16385.

46. Oleinikovas, V., Saladino, G., Cossins, B.P., and Gervasio, F.L. (2016). Understanding cryptic pocket formation in protein targets by enhanced sampling simulations. J. Am. Chem. Soc. *138*, 14257–14263.

47. Kim, C.K., Ghosh, P., Pagliuca, C., Zhu, Z., Menichetti, S., and Rotello, V.M. (2009). Entrapment of hydrophobic drugs in nanoparticle monolayers with efficient release into cancer cells. J. Am. Chem. Soc. *131*, 1360–1361.

48. Manea, F., Bindoli, C., Polizzi, S., Lay, L., and Scrimin, P. (2008). Expeditious synthesis of water-soluble, monolayer-protected gold nanoparticles of controlled size and monolayer composition. Langmuir *24*, 4120–4124.

49. Wang, J., Wolf, R.M., Caldwell, J.W., Kollman, P.A., and Case, D.A. (2004). Development and testing of a general amber force field. J. Comput. Chem. *25*, 1157–1174.

50. Bayly, C.I., Cieplak, P., Cornell, W., and Kollman, P.A. (1993). A well-behaved electrostatic potential based method using charge restraints for deriving atomic charges: the RESP model. J. Phys. Chem. *97*, 10269–10280.

51. Vanquelef, E., Simon, S., Marquant, G., Garcia, E., Klimerak, G., Delepine, J.C., Cieplak, P., and Dupradeau, F.-Y. (2011). R.E.D. Server: a web service for deriving RESP and ESP charges and building force field libraries for new molecules and molecular fragments. Nucleic Acids Res. *39*, W511–W517.

52. Heinz, H., Vaia, R.A., Farmer, B.L., and Naik, R.R. (2008). Accurate simulation of surfaces and interfaces of face-centered cubic metals using 12-6 and 9-6 Lennard-Jones potentials. J. Phys. Chem. C *112*, 17281–17290.

53. Hess, B., Kutzner, C., van der Spoel, D., and Lindahl, E. (2008). GROMACS 4: algorithms for highly efficient, load-balanced, and scalable molecular simulation. J. Chem. Theor. Comput. *4*, 435–447.